Multiresolution optical characteristics of rough sea surface in the infrared

Karine Caillault,[1,*] Sandrine Fauqueux,[1] Christophe Bourlier,[2] Pierre Simoneau,[1] and Luc Labarre[1]

[1]Department of Applied and Theoretical Optics, Office National d'Etudes et Recherches Aérospatiales, Chemin de la Hunière, 91761 Palaiseau Cedex, France

[2]Institut de recherche en électronique et électrique de Nantes Atlantique (IREENA), Ecole polytechnique de l'université de Nantes, Rue Christian Pauc, La Chantrerie, BP 50609, 44306 Nantes Cedex 3, France

*Corresponding author: karine.caillault@onera.fr

Received 28 February 2007; revised 31 May 2007; accepted 6 June 2007; posted 7 June 2007 (Doc. ID 80506); published 23 July 2007

An analytical model of sea optical properties has been developed in order to generate sea surface images, as seen by an infrared sensor. This model is based on a statistical approach and integrates the spatial variability of a wind-roughened sea surface whose variability ranges from a 1-m to a kilometer scale. It also takes into account submetric variability. A two-scale approach has been applied by superimposing small scale variability (smaller than the pixel footprint) to larger ones. Introducing multiresolution in the sensor field of view allows the requirement of any observational configuration, including nadir as well as grazing view geometry. The physical background of the methods has been tested against theoretical considerations. We also obtained a good agreement with dataset collections at our disposal and taken from the literature, such that a bias shows up at grazing angles, mainly explained by not taking into account multiple reflections. Applied to the generation of synthetic sea surface radiance images, our model leads to good quality ocean scenes, whatever the contextual conditions.

OCIS codes: 010.4450, 240.5770, 260.3060, 290.5880, 000.5490, 280.0280.

1. Introduction

Defining electro-optical systems performances requires up to date background signatures models in order to catch with the continual evolution of new optical sensors. The need of computed images including any observational configurations (nadir or grazing view geometry from ground-based, airborne or shipborne sensors) is then of a major interest. It implies the introduction of multi-resolution in the field of view and leads to develop multi-scale approaches describing background radiation variability with corresponding resolution.

In the scope of the development of a new version of the infrared background scene generator MATISSE [1] (Advanced Modeling of the Earth for the Imaging and the Simulation of the Scenes and their Environment), a model of sea surface optical properties must be implemented. It has to take into account a 1-meter spatial variability as well as a larger scale. Sub-pixel variability must also be included. All of this should moreover cover the spectral bandwidth of MATISSE extending from 765 to 3300 cm^{-1} (3 to 13 μm).

Different ways can be thought of in order to retrieve the radiative characteristics of a wind-roughened water surface. Models issued from the computer graphics literature, such as the empirical Phong's [2] model or the physical Cook-Torrance's [3] model, are based on roughness parameters. These parameters are then adjusted to fit at best the surface reflectance. Yet they are not easily connected to contextual parameters (for example wind speed and wind direction). Monte-Carlo methods [4,5] are the most accurate, but ray tracing needs a fine discretization of the sea surface (smaller than one millimeter) in order to properly take into account the capillary waves. Considering a background scene generator with a spatial extent ranging from the meter to the kilometer, algorithms based on these methods would consume too much computation time. Another well-known class of methods estimates a statistical average of local optical properties deduced from Fresnel coefficients for a given slope probability

0003-6935/07/220001-11$15.00/0

density function (PDF). In most cases, the slope of the PDF is assumed to be Gaussian [6–10]. For non-Gaussian PDF, a paper of Bourlier [11] has been recently published. Those methods give analytical expressions of optical properties. Not only they take into account contextual characteristics, such as waves from swell to capillary waves, with associated atmospheric conditions (wind, fetch), but they also include shadowing and hiding functions [12–15]. Their major drawback consists in the zero-level average sea-level implied by still assuming a centered slope of the PDF. This assumption is suitable when the pixels footprints are large enough to include the whole sea surface variability. Meanwhile it collapses when the pixel footprint only covers a small area of the sea surface. In this case a non-zero mean vector-value sea surface slope has to be considered.

In this paper, we introduce a new two-scale approach intended to calculate the sea surface optical properties. It consists in superimposing the small scale variability (smaller than the pixel footprint) to the large scale one. The analytical expressions are extended to integrate any slope mean vector-value and covariance matrix, while the statistical properties are determined for the resolution required by the observational configuration.

The paper is organized as follows. In Section 2, we first derive general analytical expressions for sea surface optical properties. They are obtained from models given in Refs. 6–10 and extended to any surface size. The different terms of the expressions, such as the shadowing functions, PDF, Fresnel coefficient and geometrical parameters, are described. Secondly, the determination of the slope statistical parameters (mean values and covariance matrix) is presented. We recall the expressions given in the literature. They are only suitable when the considered surface portion contains the whole sea surface statistics. When this condition is not fulfilled, the two-scale approach developed in this paper has to be applied. From a small scale point of view, the statistical parameters can be obtained analytically whereas a large scale will require a geometrical sea surface generation. Finally, an extension of our two-scale model based on a finer sea surface discretization is presented. Section 3 is devoted to verifications of the physical validity of our model. Conservation of energy and the convergence of optical properties from high to low resolution are investigated. In Section 4, radiance images of the ocean surface are shown to illustrate the quality of our model of optical properties and demonstrate its feasibility for extended domains. Finally, Section 5 gives concluding remarks.

2. Analytical Expressions of Optical Properties

The characteristic scales of a wind-roughened sea surface range from a few hundred meters for the swell to millimeter for the capillary waves. Curvature radius of such capillary waves being much larger than the infrared wavelength, the water surface can be seen as locally flat allowing the use of a first-order geometrical-optics approach.

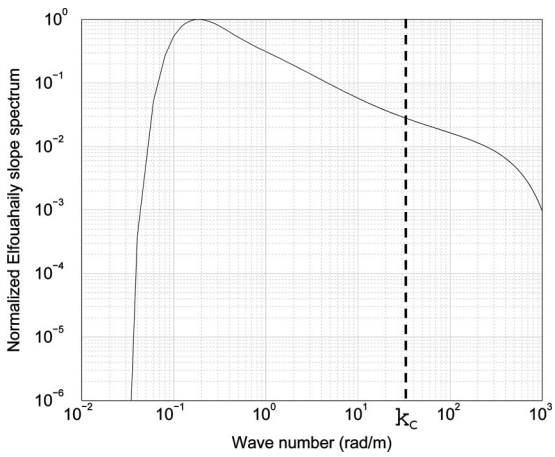

Fig. 1. Normalized omnidirectional Elfouhaily spectrum for wind velocity at 10 m above average ocean surface $u_{10} = 8\ m.s^{-1}$ and infinite fetch. The vertical dashed line indicates the location of the cutoff wavenumber k_c.

We assume that the surface slopes are governed by a stationary, ergodic and Gaussian process. Thus, it is totally defined by its mean vector-value and its autocorrelation function. For a stationary random process, the Fourier transform of the autocorrelation function is the power spectral density. In this study, the selected power spectral density is Elfouhaily's spectrum [16], whose omnidirectional component is presented in Fig. 1. This is an analytical global spectrum which covers both gravity and capillary waves. This spectrum also is in good agreement with in situ observations made by Cox and Munk [16].

In order to calculate for each pixel the effective optical properties, we introduce the *intersected rough area (IRA)* defined as the intersection of the rough surface and the pixel instantaneous field of view, containing hidden parts as well as seen ones. Figure 2 displays a schematic representation of a mono-

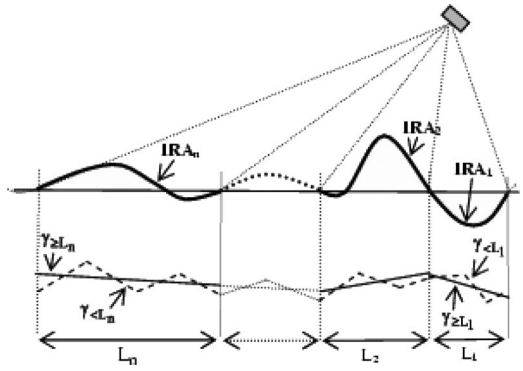

Fig. 2. Schematic representation of a mono-dimensional sea surface. In the upper part, bold line indicates the sea surface. It is decomposed into intersected rough areas (IRAs) related to pixels solid angles. In the lower part, a decomposition of the sea surface is shown: small scale waves (dashed lines) are superimposed on large scale waves (plain lines) on the n IRAs. The size of the orthogonal projection of the IRAs is given by $L_1, L_2, \ldots, L_n$. Stochastic processes describing slopes are given by $\gamma_{<L_i}$ and $\gamma_{\geq L_i}$ $(i = 1, \ldots, n)$ for the small and large scales respectively.

dimensional sea surface as seen by a sensor. For each sensor pixel, the IRA is given by the bold curve. The IRA is more or less extended, depending on the required pixel resolution and on the viewing geometry. Effective optical properties may be given as a statistical average of the local optical properties over the surface slopes observed by each pixel.

A. General Expressions

Analytical expressions of optical properties of a wind-roughened sea surface in the low resolution case are given in various references (see Refs. 6–10). Those expressions are based on the hypothesis that all the statistical information is included in the considered IRA, which means that the associated part of the sea surface has a zero-level in average. This property is not valid when a high resolution is required because one pixel of the sensor may observe in this case only a fraction of sea wave. Thus, analytical expressions must account for non-zero sea surface slope mean values. In the following, we present two-dimensional optical properties expressions based on Refs. 6–10, but extended to the general case, so that any sea surface slope mean values and variances can be used. One-dimensional expressions are detailed in Ref. 18. Monostatic and bistatic shadowing functions are also included. They model the fractional area of the sea surface illuminated and seen by the observer. Multiple reflections, however, are not considered.

For unpolarized light, we recall the Fresnel formula at the air-sea interface expressing the local reflectivity of a plane surface:

$$\rho(\theta_{inc}) = \frac{1}{2}\left(\frac{\sin^2(\theta_{inc}-\theta_t)}{\sin^2(\theta_{inc}+\theta_t)} + \frac{\tan^2(\theta_{inc}-\theta_t)}{\tan^2(\theta_{inc}+\theta_t)}\right), \quad (1)$$

$$n_a \sin\theta_{inc} = n_w \sin\theta_t, \quad (2)$$

where n_a and n_w are the spectral refractive indexes of air and sea water respectively, θ_{inc} is the incident zenith angle and θ_t is the transmission angle.

For infrared wavelengths, the law of conservation of energy and the Kirchhoff law give the local emissivity of sea surface as:

$$\varepsilon(\theta_{inc}) = 1 - \rho(\theta_{inc}). \quad (3)$$

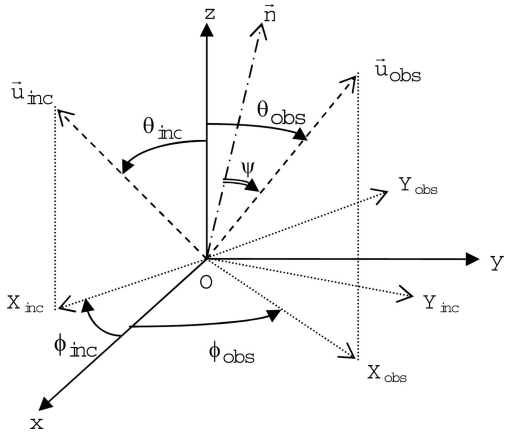

Fig. 3. Geometry definition: (0xyz) is the coordinate system relative to the upwind direction x and crosswind direction y; $\vec{u}_{obs}$ and $\vec{u}_{inc}$ are observation and incident directions respectively, defined by their zenith and azimuth angles (θ_{obs}, ϕ_{obs}) and (θ_{inc}, ϕ_{inc}) relative to the (Oxyz) coordinate system; $\vec{n}$ is the facet normal; ψ is the angle between facet normal $\vec{n}$ and observation direction $\vec{u}_{obs}$.

1. Emissivity

In the general case, effective emissivity is expressed as:

$$\tilde{\varepsilon}(\theta_{obs},\ \phi_{obs}) = \frac{\int_{-\infty}^{+\infty}\int_{-\infty}^{+\infty}[1-\rho(\psi)]\times P_{\mathbf{m},\mathbf{C}}(\gamma_x,\ \gamma_y)\times g(\theta_{obs},\ \phi_{obs};\ \gamma_x,\ \gamma_y)\times\cos\theta_{obs}\times S_{\mathbf{m},\mathbf{C}}^{\varepsilon}(\theta_{obs},\ \phi_{obs};\ \gamma_x,\ \gamma_y)d\gamma_x d\gamma_y}{\int_{-\infty}^{+\infty}\int_{-\infty}^{+\infty}P_{\mathbf{m},\mathbf{C}}(\gamma_x,\ \gamma_y)\times g(\theta_{obs},\ \phi_{obs};\ \gamma_x,\ \gamma_y)\times\cos\theta_{obs}\times S_{\mathbf{m},\mathbf{C}}^{\varepsilon}(\theta_{obs},\ \phi_{obs};\ \gamma_x,\ \gamma_y)d\gamma_x d\gamma_y}, \quad (4)$$

where $\theta_{obs} \in [-\pi/2, \pi/2]$ and $\phi_{obs} \in [0, 2\pi]$ are the zenith and azimuth observation angles (see Fig. 3 for geometry description). γ_x and γ_y are the surface slopes in the upwind and crosswind directions respectively. $\rho(\psi)$ is the unpolarized Fresnel coefficient in power with ψ the angle between the normal perpendicular to the facet and the observation direction. $g(\theta_{obs}, \phi_{obs}; \gamma_x, \gamma_y)$ is a geometrical constraint defined in Refs. 10 and 19. Considering a facet with slopes γ_x and γ_y, let S_o be its projected area in the observer plane (plane containing the observer and the normal perpendicular to the observation direction) and S_E its orthogonal projection on the ellipsoid defining Earth. We have: $g(\theta_{obs}, \phi_{obs}; \gamma_x, \gamma_y) \times \cos(\theta_{obs}) = S_o/S_E$. $P_{\mathbf{m},\mathbf{C}}(\gamma_x, \gamma_y)$ is the slopes PDF, with the slope mean vector-value $\mathbf{m}$ and the slope covariance matrix $\mathbf{C}$ expressed as:

$$\mathbf{m} = (m_x,\ m_y)^T, \quad (5a)$$

$$\mathbf{C} = \begin{pmatrix} \boldsymbol{\sigma_x}^2 & \boldsymbol{\sigma_{xy}}^2 \\ \boldsymbol{\sigma_{xy}}^2 & \boldsymbol{\sigma_y}^2 \end{pmatrix}. \quad (5b)$$

U^T denotes the transpose vector of U. m_x, m_y and $\boldsymbol{\sigma_x}^2$, $\boldsymbol{\sigma_y}^2$ are the slope mean values and slope variances in the upwind and crosswind directions. $\boldsymbol{\sigma_{xy}}^2$ is the covariance between γ_x and γ_y. $S_{\mathbf{m},\mathbf{C}}{}^{\varepsilon}(\theta_{obs}, \phi_{obs}; \gamma_x, \gamma_y)$ is the monostatic shadowing function which is defined as the ratio of the seen area to the total area subtending the surface [12].

Let's emphasize that this general expression of the effective emissivity differs from expressions found in literature by its ability to consider surface slope mean values different from zero. Thus, the parameter $\mathbf{m}$ appears in PDF and shadowing function expressions. Denominator of Eq. (4) is also of prime importance and constitutes another important difference. It evaluates the projection in observer plane of the fractional area of the sea surface seen by the pixel. The impact of this weighting parameter will be mostly seen when wave heights can not be neglected compared to the IRA projection size. Otherwise, it equals unity.

Let's note that the two-dimensional shadowing function $S_{\mathbf{m},\mathbf{C}}{}^{\varepsilon}$ depends on zenith and azimuth observation angles θ_{obs} and ϕ_{obs}. For a given ϕ_{obs}, Bourlier et al. [15] showed that the 2-D shadowing effect is obtained from the 1-D shadowing effect in the (OX_{obs}) direction characterized by the azimuth direction ϕ_{obs}. In the $(OX_{obs}Y_{obs})$ coordinate system, the surface slopes in respectively the (OX_{obs}) and (OY_{obs}) directions are expressed as:

$$\begin{aligned}\gamma_{Xobs} &= \gamma_x \cos\phi_{obs} + \gamma_y \sin\phi_{obs}\\ \gamma_{Yobs} &= -\gamma_x \sin\phi_{obs} + \gamma_y \cos\phi_{obs}.\end{aligned} \tag{6}$$

Thus, simplifying by $\cos(\theta_{obs})$, Eq. (4) becomes:

$$\tilde{\varepsilon}(\theta_{obs},\ \phi_{obs}) = \frac{\displaystyle\int_{-\infty}^{+\infty}\int_{-\infty}^{+\infty}[1-\rho(\psi)]\times P_{\mathbf{m}_{obs},\mathbf{C}_{obs}}(\gamma_{Xobs},\ \gamma_{Yobs})\times g(\theta_{obs},\ \phi_{obs};\gamma_{Xobs},\ \gamma_{Yobs})\times S_{m_{Xobs},\sigma_{Xobs}}{}^{\varepsilon}(\theta_{obs};\gamma_{Xobs})d\gamma_{Xobs}d\gamma_{Yobs}}{\displaystyle\int_{-\infty}^{+\infty}\int_{-\infty}^{+\infty}P_{\mathbf{m}_{obs},\mathbf{C}_{obs}}(\gamma_{Xobs},\ \gamma_{Yobs})\times g(\theta_{obs},\ \phi_{obs};\gamma_{Xobs},\ \gamma_{Yobs})\times S_{m_{Xobs},\sigma_{Xobs}}{}^{\varepsilon}(\theta_{obs};\gamma_{Xobs})d\gamma_{Xobs}d\gamma_{Yobs}}. \tag{7}$$

The slope vector-value $(\gamma_{Xobs}, \gamma_{Yobs})$ is also a stationary, ergodic and Gaussian process. Its PDF is $P_{\mathbf{m}_{obs},\mathbf{C}_{obs}}(\gamma_{Xobs}, \gamma_{Yobs})$ with mean $\mathbf{m}_{obs} = (m_{Xobs}, m_{Yobs})^T = \mathbf{A}_{\phi_{obs}}\mathbf{m}$ and covariance matrix $\mathbf{C}_{obs} = \mathbf{A}_{\phi_{obs}}\mathbf{C}\mathbf{A}_{\phi_{obs}}{}^T$, in which:

$$A_\phi = \begin{pmatrix}\cos\phi & \sin\phi\\ -\sin\phi & \cos\phi\end{pmatrix}. \tag{8}$$

The different terms of Eq. (7) are expressed as:

$$\psi = \cos^{-1}\left[\frac{1}{\sqrt{1+\gamma_{Xobs}{}^2+\gamma_{Yobs}{}^2}}(\cos\theta_{obs} - \gamma_{Xobs}\sin\theta_{obs})\right], \tag{9a}$$

$$g(\theta_{obs},\ \phi_{obs};\ \gamma_{Xobs},\ \gamma_{Yobs}) = 1 - \gamma_{Xobs}\tan\theta_{obs}. \tag{9b}$$

The monostatic shadowing function is given by the uncorrelated monostatic Smith shadowing function [13] which has been extended to non-zero PDF:

$$S_{m,\sigma}{}^{\varepsilon}(\theta;\gamma) = \begin{cases}\dfrac{\Uparrow_{(-\infty;\cot an\ \theta]}(\gamma)}{1+\Lambda_{m,\sigma}(\theta)} & \text{if } \theta \ge 0\\ \dfrac{\Uparrow_{[\cot an\ \theta;+\infty)}(\gamma)}{1+\Lambda_{m,\sigma}(\theta)} & \text{if } \theta \le 0\end{cases}, \tag{9c}$$

where: θ is zenith angle,

$$\Uparrow_I(x) = \begin{cases}1 & \text{if } x \in I\\ 0 & \text{otherwise,}\end{cases}$$

$$\text{where } I = \begin{cases}(-\infty;\ \cot an\ \theta] & \text{if } \theta \ge 0\\ [\cot an\ \theta;\ +\infty) & \text{if } \theta \le 0,\end{cases} \tag{9d}$$

$$\Lambda_{m,\sigma}(\theta) = \begin{cases}\displaystyle\int_{\cot an\ \theta}^{+\infty}(\gamma\tan\theta - 1)P_{m,\sigma}(\gamma)d\gamma & \text{if } \theta \ge 0\\ \displaystyle\int_{-\infty}^{\cot an\ \theta}(\gamma\tan\theta - 1)P_{m,\sigma}(\gamma)d\gamma & \text{if } \theta \le 0\end{cases}. \tag{9e}$$

The uncorrelated monostatic Smith shadowing function relies on the assumption that surface heights and slopes are uncorrelated. Thus, optical properties expressions depend only on slopes.

Finally, g and $S_{m_{Xobs},\sigma_{Xobs}}{}^{\varepsilon}$ depending only on γ_{Xobs}, the denominator of Eq. (7) becomes, after integrating upon γ_{Yobs}:

$$D = 1 - \frac{m_{Xobs}\tan(\theta_{obs})}{1+\Lambda_{m_{Xobs},\sigma_{Xobs}}(\theta_{obs})}. \tag{10}$$

We note that a second integration upon γ_{Yobs} is necessary to calculate the numerator of Eq. (7), due to the dependence of ψ with γ_{Yobs}. As presented in Ref. 11, the variance ${\sigma_{Yobs}}^2$ associated to γ_{Yobs} being much smaller than $1 + {\gamma_{Xobs}}^2 + {m_{Yobs}}^2$, one can approximate ψ by:

$$\cos(\psi) \approx \cos(\psi') = \frac{1}{\sqrt{1 + {\gamma_{Xobs}}^2 + {m_{Yobs}}^2}} \times (\cos\theta_{obs} - \gamma_{Xobs}\sin\theta_{obs}). \quad (11)$$

Thus, Eq. (7) can be written as:

$$\tilde{\varepsilon}(\theta_{obs}, \phi_{obs}) \approx \frac{\int_{-\infty}^{+\infty} [1 - \rho(\psi')] \times P_{m_{Xobs},\sigma_{Xobs}}(\gamma_{Xobs}) \times (1 - \gamma_{Xobs}\tan\theta_{obs}) \times {S_{m_{Xobs},\sigma_{Xobs}}}^{\varepsilon}(\theta_{obs}; \gamma_{Xobs}) d\gamma_{Xobs}}{1 - \frac{m_{Xobs}\tan(\theta_{obs})}{1+\Lambda_{m_{Xobs},\sigma_{Xobs}}(\theta_{obs})}}. \quad (12)$$

This approximation leads to a large gain of computational time without a noticeable loss of accuracy when the emissivity is estimated. For example, if $\mathbf{m} = (0.15, -0.15)$ and $\mathbf{C}$, for $u_{10} = 10\ m.s^{-1}$, is such that $\sigma_x = 0.19$, $\sigma_{xy} = 0$ and $\sigma_y = 0.16$, we verified that the computation time was reduced by a factor 30 while a loss of accuracy of less than 1%.

2. Reflectivity

Extending expressions given in Refs. 6–10 to the general case by considering any slope mean vector-value and covariance matrix and by normalizing by D, the effective reflectivity becomes:

The two-dimensional shadowing function is now the uncorrelated bistatic Smith shadowing function [13] ${S_{\mathbf{m},\mathbf{C}}}^{\rho}(\theta_{inc}, \phi_{inc}; \theta_{obs}, \phi_{obs}; \gamma_x, \gamma_y)$. As previously, it can be expressed from the 1-D case [15]:

$${S_{m_X,\sigma_X}}^{\rho}(\theta_{inc}; \theta_{obs}; \gamma_{Xobs}, \gamma_{Xinc}) = \frac{1}{1 + \Lambda_{m_{Xobs},\sigma_{obs}}(\theta_{obs}) + \Lambda_{m_{Xinc},\sigma_{inc}}(\theta_{inc})}, \quad (14c)$$

where m_{Xinc} is the slopes mean in (OX_{inc}) directions.

As in Ref. 20, we use this shadowing function expression instead of the expression given in Ref. 9, which does not guarantee the continuity of reflectivity. Indeed, incidence angles can as well be expressed as $(\theta_{inc}, \phi_{inc})$ or $(-\theta_{inc}, \phi_{inc} + \pi)$. Fixing in the expression given by Ref. 9, $\theta_{inc}\theta_{obs} > 0$ and $|\theta_{inc}| > |\theta_{obs}|$, then $(\theta_{inc}, \phi_{inc})$ leads to a bistatic shadowing function equals to $[1 + \Lambda_{m_{Xinc},\sigma_{inc}}(\theta_{inc})]^{-1}$ whereas $(-\theta_{inc}, \phi_{inc} + \pi)$ leads to $[1 + \Lambda_{m_{Xobs},\sigma_{obs}}(\theta_{obs}) + \Lambda_{m_{Xinc},\sigma_{inc}}(\theta_{inc})]^{-1}$.

Finally, the Jacobian J resulting from the variables transformation from slopes to incident angles is:

$$J = \frac{1 + \cos\theta_{inc}\cos\theta_{obs} + \sin\theta_{inc}\sin\theta_{obs}\cos(\phi_{obs} - \phi_{inc})}{(\cos\theta_{inc} + \cos\theta_{obs})^3}. \quad (14d)$$

$$\tilde{\rho}(\theta_{inc}, \phi_{inc}; \theta_{obs}, \phi_{obs}) = \frac{\rho[\psi(\theta_{obs}, \phi_{obs}; \gamma_{x0}, \gamma_{y0})] \times P_{\mathbf{m},\mathbf{C}}(\gamma_{x0}, \gamma_{y0}) \times g(\theta_{obs}, \phi_{obs}; \gamma_{x0}, \gamma_{y0}) \times {S_{\mathbf{m},\mathbf{C}}}^{\rho}(\theta_{inc}, \phi_{inc}; \theta_{obs}, \phi_{obs}; \gamma_{x0}, \gamma_{y0}) \times |J|}{1 - \frac{m_{Xobs}\tan(\theta_{obs})}{1+\Lambda_{m_{Xobs},\sigma_{Xobs}}(\theta_{obs})}}. \quad (13)$$

Each term of Eq. (13) is defined as it was in Eq. (4), with (γ_x, γ_y) replaced by $(\gamma_{x0}, \gamma_{y0})$. The couple $(\gamma_{x0}, \gamma_{y0})$ describes the specular direction $\theta_{obs} = -\theta_{inc}$ and $\phi_{obs} = \phi_{inc}$. We have:

$$\gamma_{x0} = -\frac{\sin\theta_{obs}\cos\phi_{obs} + \sin\theta_{inc}\cos\phi_{inc}}{\cos\theta_{inc} + \cos\theta_{obs}}, \quad (14a)$$

$$\gamma_{y0} = -\frac{\sin\theta_{obs}\sin\phi_{obs} + \sin\theta_{inc}\sin\phi_{inc}}{\cos\theta_{inc} + \cos\theta_{obs}}. \quad (14b)$$

B. Statistical Parameters

Estimating the optical properties implies the knowledge of the slope statistical parameters for each IRA constituting the sensor footprint. Two configurations can be encountered depending on the pixel resolution and the associated slope statistical information: the low resolution case, where the considered IRA is extended enough to reach the whole sea surface statistical information, and the high resolution case.

1. Low Resolution Case

In this case, the IRA size is large enough to consider that the whole statistical information is included in one realization of the Gaussian stochastic process describing slopes on the IRA. Slope mean values in the upwind and crosswind directions are thus $\mathbf{m} = (m_x, m_y) = \mathbf{0}$, while matrix covariance components are given by:

$$\begin{aligned}
\sigma_x^2 &= \int_0^{+\infty}\int_{-\pi}^{\pi} k^2 \cos^2\theta S(k,\theta)\,d\theta\,dk,\\
\sigma_y^2 &= \int_0^{+\infty}\int_{-\pi}^{\pi} k^2 \sin^2\theta S(k,\theta)\,d\theta\,dk,\\
\sigma_{xy}^2 &= 0,
\end{aligned} \tag{15}$$

where $S(k,\theta)$ is Elfouhaily *et al.* [16] height spectrum, with k the wave number and θ the wave propagation direction with respect to the wind direction. Then, slopes relative to incident direction (OX_{inc}) and observation direction (OX_{obs}) have zero mean values. The denominator D given by Eq. (10), equal to 1, disappears and we retrieve the low resolution expressions given by Refs. 6–10.

2. High Resolution Case

To estimate high resolution optical properties, mean vector-value and covariance matrix of the sea surface slopes have to be calculated for the IRA. In this case, the IRA being not extended enough to contain the whole statistical information of the surface slopes, the slope mean vector-value is not equal to zero and the components of the covariance matrix cannot be obtained by integrating the sea surface spectrum over all real wavenumbers. Thus we assume that the stochastic process describing slopes on an IRA can be decomposed into two independent components related to sub-IRA and over-IRA variability respectively. This is the main idea of our two-scale approach. It implies the introduction of a cutoff wavenumber $k_c = \pi/L$ (see Fig. 1), where L is the size of the orthogonal projection of the IRA on the ellipsoid defining the Earth. The cutoff wavenumber is defined in agreement with the anti-aliasing criteria for a L-meters discretization step. Wavenumbers larger than k_c are used in order to describe small scales whose associated waves will be defined as small scale waves. On the other hand, large scale waves are associated to the scales described by wavenumbers smaller than k_c. The two considered components $\gamma_{<L}$ (small scale) and $\gamma_{\geq L}$ (large scale) are stationary, ergodic and Gaussian processes whose spectrum is defined by the Elfouhaily spectrum restricted to $|k| > k_c$ (small scale) and $|k| \leq k_c$ (large scale) respectively. Figure 2 shows a schematic representation of the sea surface composed of n IRAs. The lower part of the figure gives the decomposition of the sea surface in two scales where large scale waves are given by plain lines and small scale waves by dashed lines.

Sea surface slopes can thus be written as:

$$\gamma = \gamma_{\geq L} + \gamma_{<L}. \tag{16}$$

We assume that the whole statistics of slopes relative to wavenumbers $|k| > k_c$ is included in all IRAs whose projection sizes are greater than L meters. Thus, a realisation of $\gamma_{<L}$ on the considered IRA has a Gaussian distribution with slope mean vector-value $\mathbf{m}_{<L}$ and covariance matrix $\mathbf{C}_{<L}$, where:

$$\begin{aligned}
\mathbf{m}_{<L} &= 0,\\
\sigma_{x;<L}^2 &= \int_{k_c}^{+\infty}\int_{-\pi}^{-\pi} k^2 \cos^2(\theta) S(k,\theta)\,d\theta\,dk,\\
\sigma_{y;<L}^2 &= \int_{k_c}^{+\infty}\int_{-\pi}^{-\pi} k^2 \sin^2(\theta) S(k,\theta)\,d\theta\,dk,\\
\sigma_{xy;<L}^2 &= 0.
\end{aligned} \tag{17}$$

On the contrary, a realisation of $\gamma_{\geq L}$ on the considered IRA does not reach its whole statistics. It is thus necessary to simulate $\gamma_{\geq L}$ and calculate slope mean vector-value $\mathbf{m}_{\geq L}$ and covariance matrix $\mathbf{C}_{\geq L}$. Simulating $\gamma_{\geq L}$ is equivalent to geometrically generate sea slopes with wavenumbers $|k| \leq k_c$. Slopes are built by means of a spectral method [21,22] using the Elfouhaily spectrum restricted to $|k| \leq k_c$, so the coherence with the calculation of statistical properties of $\gamma_{<L}$ will be guaranteed. The selected method of surface slope generation consists in summing sinusoids with adequate amplitude and phase. For each IRA, one slope vector-value is generated, setting the discretization step to L, the IRA projection size. Moreover, we note that in the whole sensor footprint, a variable discretization step has to be used. The FFT approach requiring a constant step cannot then be applied.

The slope mean vector-value $\mathbf{m}_{\geq L}$ is equal to the slope of the IRA, while all the coefficients of the slope covariance matrix $\mathbf{C}_{\geq L}$ are equal to zero. We will call this approach the Variable Step method. Finally, given the assumption of independence of the two processes, slope mean vector-value and covariance matrix of the total process can be written as:

$$\begin{aligned}
\mathbf{m} &= \mathbf{m}_{\geq L} + \mathbf{m}_{<L} = \mathbf{m}_{\geq L},\\
\mathbf{C} &= \mathbf{C}_{\geq L} + \mathbf{C}_{<L} = \mathbf{C}_{<L}.
\end{aligned} \tag{18}$$

Let's point out that the surface generation method takes the time into account. $\gamma_{<L}$ being ergodic, the temporal evolution of the statistical parameters is coherent and so are the associated optical properties.

3. Extension of the Variable Step Model

As we have seen previously, in the Variable Step approach the discretization step Δ is set to L. If one considers that this discretization is too coarse, one can reduce the discretization step to $\Delta = L/2^n$, with $n \in \{1, 2, \ldots\}$ and such as $\Delta \geq 1$ m, one meter being the smallest spatial resolution required in the scope of MATISSE-v2.0. This leads to $k_c = 2^n\pi/L$. In a practical point of view, a L-size facet will be subdivided in $2^n \times 2^n$ sub-facets. As in the Variable Step model, the slopes are decomposed taking into account the relation $\boldsymbol{\gamma} = \boldsymbol{\gamma}_{\geq\Delta} + \boldsymbol{\gamma}_{<\Delta}$. Mean vector-value $\mathbf{m}_{<\Delta}$ and covariance matrix $\mathbf{C}_{<\Delta}$ are also given by Eq. (17) where L is replaced by Δ. To estimate $\mathbf{m}_{\geq\Delta}$ and $\mathbf{C}_{\geq\Delta}$, slopes are generated with the discretization step Δ for the $2^n \times 2^n$ sub-facets. $\mathbf{m}_{\geq\Delta}$ is thus the mean vector-value of the $2^n \times 2^n$ sub-facets slopes and $\mathbf{C}_{\geq\Delta}$ is their covariance matrix. The analytical expressions of the optical properties are then applied in the same way as in the Variable Step approach with:

$$\begin{aligned} \mathbf{m} &= \mathbf{m}_{\geq\Delta} + \mathbf{m}_{<\Delta}, \\ \mathbf{C} &= \mathbf{C}_{\geq\Delta} + \mathbf{C}_{<\Delta}. \end{aligned} \tag{19}$$

This method is called the Variable Step $L/2^n$ model.

Another extension is the 1 Meter Step model defined as follows. For each IRA with a projection size L, n can be chosen such as 2^n is equal to L. Thus, the discretization step is fixed to $\Delta = 1$ m ($k_c = \pi$) for the whole sensor footprint. $\mathbf{m}_{<1\,\mathrm{m}}$ and $\mathbf{C}_{<1\,\mathrm{m}}$ are estimated only once from Eq. (17). As previously, $\mathbf{m}_{\geq 1\,\mathrm{m}}$ and $\mathbf{C}_{\geq 1\,\mathrm{m}}$ are calculated as the mean vector-value and covariance matrix of the $2^n \times 2^n$ 1-meter slopes. In order to decrease the computation time relative to this case, we recommend to take advantage of the constant space step and to generate the sea surface by means of a spectral method based on a FFT algorithm.

3. Verifications and Comparisons

Comparisons of low resolution analytical emissivity with measurements have been achieved in Ref. 11, on dataset collected during the oceanographic cruise in the Gulf of Mexico on 16 January 1995 described in Ref. 23. Comparisons have also been done between low resolution analytical Bidirectional Reflectance Distribution Function (BRDF) and measurements performed at the COVE platform on the 6th of January 2001. They are reported in Ref. 20. The BRDF and the reflectivity defined by Eq. (13) are linked by the relation:

$$\tilde{\rho}(\theta_i,\ \phi_i;\ \theta_o,\ \phi_o) = f(\theta_i,\ \phi_i;\ \theta_o,\ \phi_o) \times \cos\theta_i. \tag{20}$$

These comparisons show a good agreement between analytical models and measurements.

From an experimental point of view, measurements of ocean radiation are not instantaneous. In the campaign described by Ref. 11, integration times range from 2 to 3.5 min and in the Ref. 20 the measurements are averaged half-hourly. So these datasets always deal with low resolution optical properties, due to the ergodicity of the considered Gaussian process.

To our knowledge, high resolution measurements have not been published. Thus, comparisons could not be conducted in the high resolution case. Field measurements for the model validation are under planning. This campaign will involve ships as well as ground stations. However, in order to ensure that our model gives correct optical properties at any resolution, we have verified that the law of conservation of energy is retrieved for various IRA sizes, as it is a strong constraint on the optical properties. Moreover, we have checked that high resolution optical properties converge to low resolution ones when pixel size increases. This exhibits the coherence between the low and high resolution expressions.

A. Conservation of Energy

The law of conservation of energy, valid for local radiative properties (see Eq. (3)), has also to be verified for average optical properties. In that case, it is expressed as:

$$\tilde{\varepsilon}(\theta_{inc},\ \phi_{inc}) + \int_{-\pi/2}^{\pi/2}\int_{0}^{\pi} \tilde{\rho}(\theta,\ \phi;\ \theta_{inc},\ \phi_{inc})\sin\theta\, d\theta\, d\phi = 1, \tag{21}$$

and must be fulfilled whatever the IRA projection size is.

Figure 4 shows Eq. (21) results as a function of incident zenith and azimuth angles. A loss of energy occurs at large zenith angles partially caused by the neglected multiple reflections. Indeed, in their sea surface emissivity model Wu and Smith [24] accounted for the direct emission intercepted by the surface and reflected in the view direction, often called the surface-emitted/surface-reflected (SESR) contribution. They have been able to validate it against sea surface emissivity measurements made by Smith et al. [23] in the Gulf of Mexico. Watts et al. [25] included in their model both SESR contribution and the second interception by the surface of an already-reflected ray, defined as the surface-reflected/surface-reflected (SRSR) contribution. They pointed out that multiple reflection effects becomes significant at high zenith angles and wind speeds. Recent studies [26,27] have implemented multiple reflection effects in the determination of the emissivity. They showed that the double reflection has to be taken into account for emission zenith angles ranging from 50° (this value decreases when the wind speed increases) to 85°.

For small IRA projection sizes we also observe that the results obtained by applying Eq. (21) are not symmetric with respect to the nadir angle $\theta = 0°$. In that case, slope mean values m_x and m_y are different from

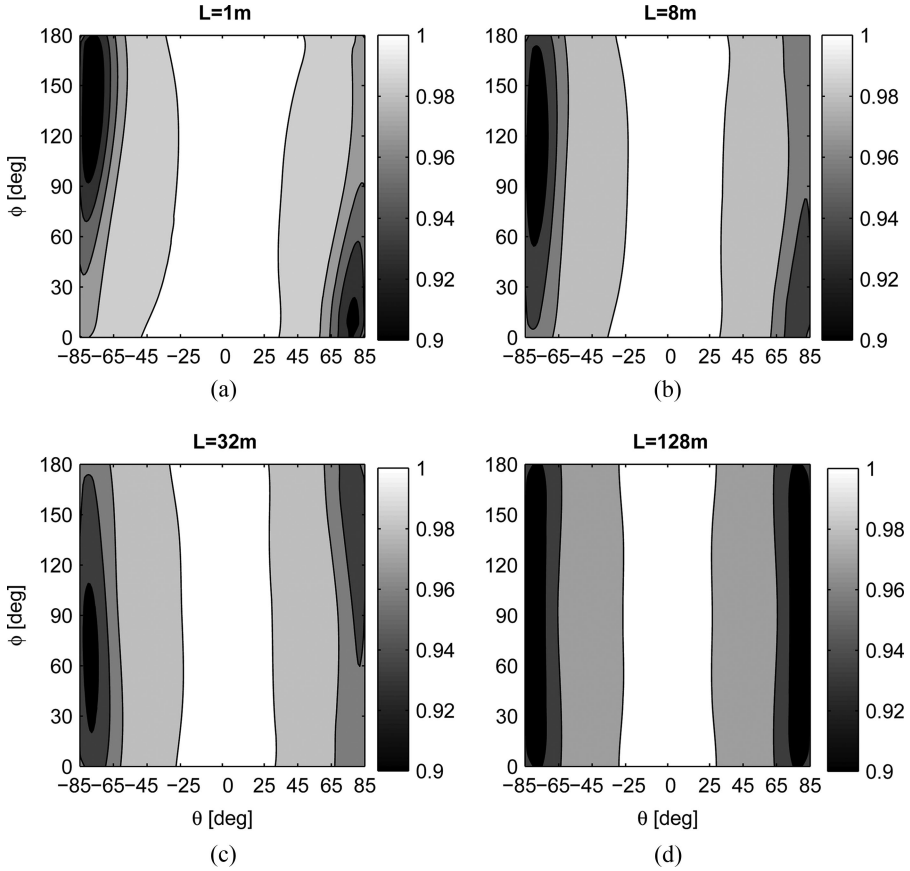

Fig. 4. Verification of the conservation of energy. Wind speed is $u_{10} = 10$ m.s^{-1}, wavelength is $\lambda = 4$ μm and four IRA projection sizes are presented: (a) L = 1 m, (b) L = 8 m, (c) L = 32 m, and (d) L = 128 m.

zero. Table 1 gives slope mean values relative to the IRA projection sizes presented in Fig. 4. Optical properties are not symmetric and so is the energy distribution. When IRA projection size increases, slopes mean vector-value **m** decreases. It even equals zero when IRA projection size becomes large enough to contain the whole statistical information of the sea surface (for L = 128 m in our example). In the same time, optical properties and energy distribution become symmetric, which is in agreement with results that would be obtained for a zero-level surface.

B. Convergence from High to Low Resolution

When IRA projection size L increases, the cutoff wavenumber $k_c = \pi/L$ becomes smaller, then more surface statistical information becomes included in $\gamma_{<L}$ (see Eq. (17) for variance expression). At the limit $k_c \to 0$, $\gamma_{<L}$ contains all the statistical information on the slopes of the sea surface and the low resolution covariance matrix is retrieved. In the same time, less statistical information is included in $\gamma_{\geq L}$, slope mean values decrease and tend towards zero, which is the low resolution case. Figures 5 and 6 show the convergence of respectively effective emissivity and reflectivity from high to low resolution case when surface size increases, for two different wind speeds. Sea surface has been generated (large scale waves) with the

Table 1. Slope Means Upwind (m_x) and Crosswind (m_y) Relative to the Surface Sizes Presented in Fig. 4

Size	L = 1 m	L = 8 m	L = 32 m	L = 128 m
m_x	0.103	0.038	−0.034	0.000
m_y	−0.052	−0.059	−0.038	0.000

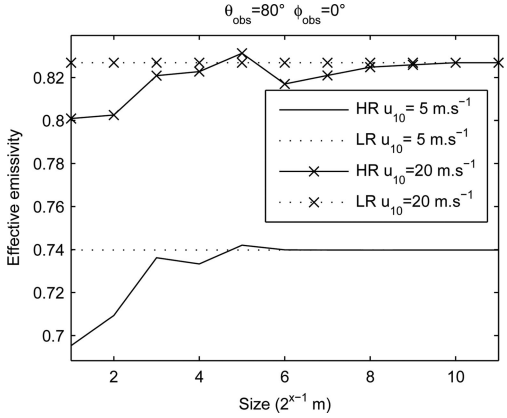

Fig. 5. Effective emissivity as a function of surface size, expressed as $L = 2^{x-1}$ m, x = 1, . . . , 11, for $\lambda = 4$ μm, two wind speeds $u_{10} = 5$ and 20 m.s^{-1} and ($\theta_{obs} = 80°$; $\phi_{obs} = 0°$). Dotted and solid lines refer to calculations done with low resolution (LR) and high resolution (HR) expressions respectively.

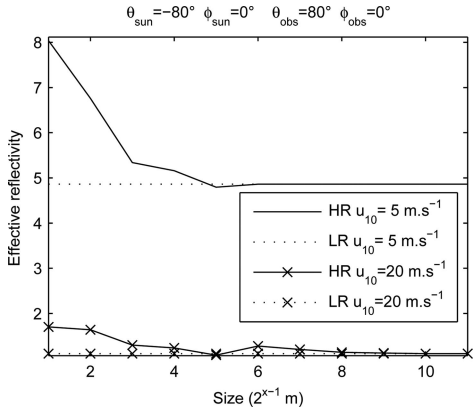

Fig. 6. Effective reflectivity as a function of surface size, expressed as $L = 2^{x-1}$ m, $x = 1, \ldots, 11$, for $\lambda = 4$ μm, two wind speeds $u_{10} = 5$ and 20 m.s^{-1} and for ($\theta_{inc} = -80°$; $\phi_{inc} = 0°$) and ($\theta_{obs} = 80°$; $\phi_{obs} = 0°$). Dotted and solid lines refer to calculations done with low resolution (LR) and high resolution (HR) expressions respectively.

same seed for the two wind speeds. Low resolution optical properties, including the whole surface variability, are represented by a straight dotted line. Convergence of high resolution optical properties depends on wind speed. Indeed, higher the wind speed is, later the convergence is reached. In the presented case, convergence is reached when surface size exceeds $2^6 = 64$ m for the low wind speed and $2^9 = 512$ m for the high wind speed. For the same wind speed value, if sea surface is generated with other seeds, convergence is also reached around the same pixel footprint size.

4. Images of Ocean Surface

We present images of sea surface radiance obtained with our model of effective optical properties. The model is implemented as a prototype before its integration in the Matisse-v2.0 code. A multi-resolution architectural solution, based on clipmaps method [28], is also implemented. It efficiently deals with levels of details consistent with the scene observation context. It relies on nested regular grids, composed of facets whose sizes are proportional to the sensor distance. Thus, objects far away from the sensor are not described with the same level of details as the ones closed by.

Sea surface radiance is given by:

$$\begin{aligned} L(\theta_{obs}, \phi_{obs}) = & \int_{\Omega_{sun}} f(\theta_{sun}, \phi_{sun}; \theta_{obs}, \phi_{obs}) \\ & \cdot \cos\theta_{sun} \cdot L_{sun}(\theta_{sun}, \phi_{sun}) \cdot d\Omega_{sun} \\ & + \int_{\Omega^+} f(\theta^+, \phi^+; \theta_{obs}, \phi_{obs}) \cdot \cos\theta^+ \\ & \cdot L_{atm}(\theta^+, \phi^+) \cdot d\Omega^+ \\ & + \tilde{\varepsilon}(\theta_{obs}, \phi_{obs}) \cdot L_{BB}(T_{sea}). \end{aligned} \quad (22)$$

where f is the BRDF.

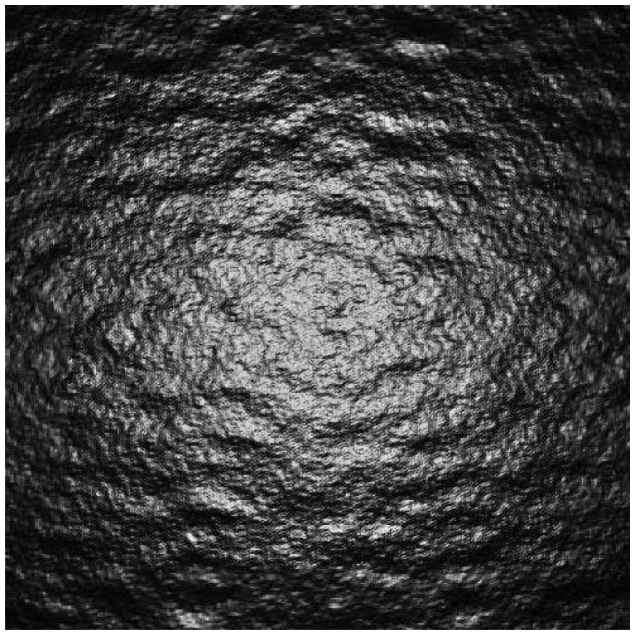

Fig. 7. Image of sea surface radiance at 4 μm composed of 500 × 500 pixels. The sensor is located at an altitude of 0.389 km and looks at nadir. The sun is at zenith. The wind speed is $u_{10} = 10$ m.s^{-1}.

The first term of Eq. (22) is the reflected solar radiance where the sun radiance is L_{sun} and Ω_{sun} is the solar solid angle; the second term is the reflected atmospheric radiance with the atmospheric radiance L_{atm} and Ω^+ the upper hemisphere; the last term is

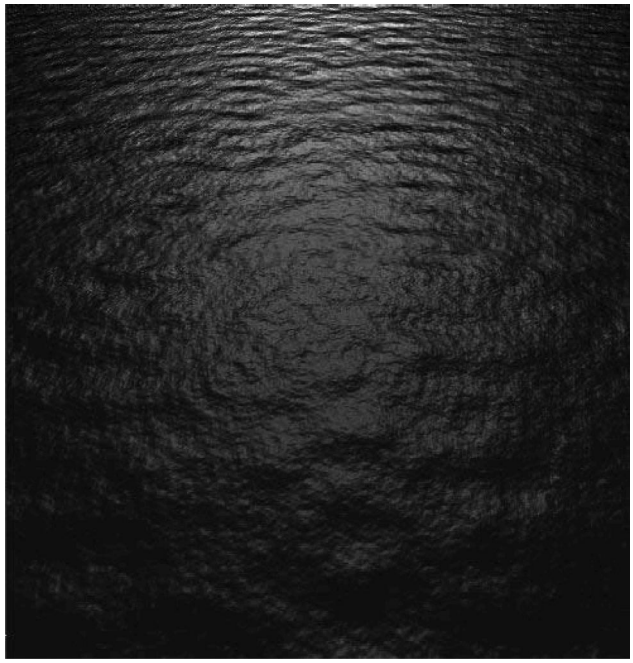

Fig. 8. Same as Fig. 7 but with the sensor located at an altitude of 0.5 km. Sensor observation angles are ($\theta_{obs} = 36°$; $\phi_{obs} = 0°$) and sun angles are ($\theta_{inc} = 40°$; $\phi_{inc} = 180°$). The wind speed is $u_{10} = 15$ m.s^{-1}.

Fig. 9. Same as Fig. 8 but with the sensor located at an altitude of 1.5 km.

the emitted radiance where $L_{BB}(T_{sea})$ is the black body radiance at sea temperature T_{sea}.

In the prototype, in order to simplify Eq. (22), the sun is assumed to be a collimated source and the atmospheric radiance to be isotropic. This does not change the purpose of our study and avoids the calculation of the integrations of the two first terms. Moreover, by introducing the law of conservation of energy in both the second term and relation (20), Eq. (22) becomes:

$$L(\theta_{obs}, \phi_{obs}) = \tilde{\rho}(\theta_{sun}, \phi_{sun}; \theta_{obs}, \phi_{obs}) \cdot L_{sun}(\theta_{sun}, \phi_{sun}) + [1 - \tilde{\varepsilon}(\theta_{obs}, \phi_{obs})] \cdot \bar{L}_{atm} + \tilde{\varepsilon}(\theta_{obs}, \phi_{obs}) \cdot L_{BB}(T_{sea}), \quad (23)$$

where $\bar{L}_{atm}$ is the isotropic atmospheric radiance value.

Figures 7 to 9 show images of the sea surface radiance obtained from our model, at 4 μm for a wind direction orthogonal to the observation direction. The sea surface temperature T_{sea} is 288 K. In Fig. 7, the wind speed is set to $u_{10} = 10$ m.s^{-1}. Sun being at zenith and sensor looking at nadir, the rendering of solar glitter pattern is well done. Due to the observational configuration, two levels corresponding to high resolution case are displayed: 1 m in the central part of the image and 2 m otherwise. Figure 10(a) shows a representation of these levels with the associated domain sizes. The outer square corresponds to the edge of the image displayed in Fig. 7. In Fig. 8, the wind speed is $u_{10} = 15$ m.s^{-1}. The sensor (altitude 0.5 km) is opposite to the sun and the zenith angles are $\theta_{obs} = 36°$ and $\theta_{inc} = 40°$. In that case, three levels of spatial resolution can be observed: 2 m in the lower part of the image, 4 m in the central part and 8 m in the upper part. Figure 9 is obtained with the same configuration as in Fig. 8, except the sensor altitude is higher (1.5 km). Thus, the levels of spatial resolutions displayed are larger: 8, 16 and 32 m from the lower part of the image to the upper part (see Figs. 10(b) and 10(c) for the associated diagrams and sizes).

On these images, we can see that the spatial variability is well retrieved. They also show that the multi-resolution is correctly taken into account in the sensor field of view and that the transition between two levels of resolution is smooth and does not add artifacts.

5. Conclusion

An analytical model of infrared optical properties has been developed to take into account the spatial variability of a Gaussian wind-roughened sea surface from 1-meter to large scale, including sub-pixel variability. It is based on a two-scale approach, called the Variable Step method, that consists in superimposing the small scale variability (smaller than the size of

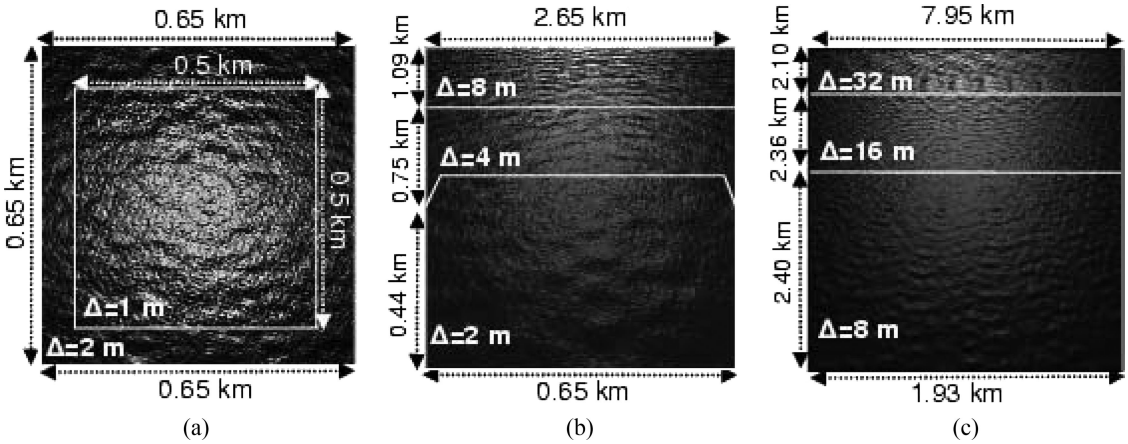

Fig. 10. Levels of spatial resolution associated with images of sea surface radiance. Sizes of each domain and related spatial resolutions are also indicated. Diagrams (a), (b), and (c) give domains and sizes related to Figs. 7, 8, and 9, respectively.

the considered IRA) to a larger one. Thus, statistical properties are calculated for the IRA whose sizes are dictated by the observational configuration. The main assumption is that the surface is governed by a stationary, ergodic and Gaussian process. The chosen spectrum is an Elfouhaily spectrum describing swell to capillary waves. Local characteristics, i.e. wind speed and direction and fetch, are input data of the selected spectrum. First-order geometrical-optics approximation is used and shadowing and hiding functions are included. Contribution from multiple reflections is not taken into account. Extensions of the Variable Step approach, based on a finer surface discretization, are also presented.

Physical validity of the proposed model is verified. The observed negative biases at grazing angles are mainly caused by neglecting multiple reflections. The implementation of our model for the generation of images of synthetic sea surface radiance shows its ability to produce good quality ocean scenes in various contextual conditions. Moreover, multi-resolution being introduced in the sensor field of view, the requirement in computing images of any observational configuration is fulfilled.

This Variable Step model will be implemented in the new version of MATISSE-v2.0.

Funds for this research have been provided by DGA/SPN, the French Armament Procurement Organization.

References

1. P. Simoneau, R. Berton, K. Caillault, S. Fauqueux, T. Huet, J. C. Krapez, L. Labarre, C. Malherbe, C. Martin, C. Miesch, and A. Roblin, "MATISSE, Version 1.2 and future developments," in *Twenty-seventh Annual Review of Atmospheric Transmission Models* (National Heritage Museum, Lexington, Mass. 2006).
2. B. T. Phong, "Illumination for computer generated pictures," Commun. ACM **18,** 311–377 (1975).
3. R. L. Cook and K. E. Torrance, "A reflectance model for computer graphics," ACM Trans. Graphics **1,** 7–24 (1982).
4. R. W. Preisendorfer and C. D. Mobley, "Albedos and glitter patterns of a wind-roughened sea surface," J. Phys. Oceanogr. **16,** 1293–1316 (1986).
5. B. G. Henderson, J. Theiler, and P. V. Villeneuve, "The polarized emissivity of a wind-roughened sea surface: a Monte-Carlo model," Rem. Sens. Environ. **88,** 453–467 (2003).
6. K. Yoshimori, K. Itoh, and Y. Ichioka, "Thermal radiative and reflective characteristics of a wind-roughened water surface," J. Opt. Soc. Am. A **11,** 1886–1893 (1994).
7. K. Yoshimori, K. Itoh, and Y. Ichioka, "Optical characteristics of a wind-roughened water surface: a two-dimensional theory," Appl. Opt. **34,** 6236–6247 (1997).
8. C. Bourlier, J. Saillard, and G. Berginc, "Intrinsic infrared radiation of the sea surface," in *Progress in Electromagnetics Research,* J. A. Kong, ed. (EMW Publishing, 2000), Vol. 27, pp. 185–335.
9. C. Bourlier, J. Saillard, and G. Berginc, "Theoretical study on two-dimensional Gaussian rough sea surface emission and reflection in the infrared frequencies with shadowing effects," IEEE Trans. Geosci. Remote Sens. **39,** 319–392 (2001).
10. C. R. Zeisse, "Radiance of the ocean horizon," J. Opt. Soc. Am. A **12,** 2022–2030 (1995).
11. C. Bourlier, "Unpolarized infrared emissivity with shadow from anisotropic rough sea surfaces with non-Gaussian statistics," Appl. Opt. **44,** 4335–4349 (2005).
12. P. Beckmann, "Shadowing of random rough surfaces," IEEE Trans. Antennas Propag. **13,** 384–388 (1965).
13. B. G. Smith, "Geometrical shadowing of random rough surface," IEEE Trans. Antennas Propag. **15,** 668–671 (1967).
14. R. J. Wagner, "Shadowing of randomly rough surfaces," J. Acoust. Soc. Am. **41,** 138–147 (1966).
15. C. Bourlier and G. Berginc, "Shadowing function with single reflection from anisotropic Gaussian rough surface. Application to Gaussian, Lorentzian and sea correlations," Waves Random Media **13,** 27–58 (2003).
16. T. Elfouhaily, B. Chapron, K. Katsaros, and D. Vandemark, "A unified directional spectrum for long and short wind-driven waves," J. Geophys. Res. **102,** 15781–15796 (1997).
17. C. S. Cox and W. H. Munk, "Measurements of the roughness of the sea surface from photographs of the sun's glitter," J. Opt. Soc. Am. **44,** 838–850 (1954).
18. K. Caillault, S. Fauqueux, C. Bourlier, and P. Simoneau, "Infrared multiscale sea surface modeling," Proc. SPIE **6360,** 636006 (2006).
19. J. Theiler and B. G. Henderson, "Geometrical constraint on shadowing in rough surface," in *Infrared Spaceborne Remote Sensing V,* M. Strojnik and B. F. Andresen, eds., Proc. SPIE **3122,** 271–279 (1997).
20. V. Ross, D. Dion, and G. Potvin, "Detailed analytical approach to the Gaussian surface bidirectional reflectance distribution function specular component applied to the sea surface," J. Opt. Soc. Am. **22,** 2442–2453 (2005).
21. F. Poirion and C. Soize, "Simulation numérique de champs vectoriels stochastiques gaussiens homogènes et non homogènes," Rech. Aérosp. **1,** 41–61 (1989).
22. A. Fournier and W. T. Reeves, "A simple model of ocean waves," ACM SIGGRAPH Comput. Graph. **20,** 75–82 (1986).
23. W. L. Smith, R. O. Knuteson, H. E. Revercomb, J. Brown, O. Brown, W. Feltz, H. B. Howell, W. McKeown, W. P. Menzel, P. Minnett, and N. R. Nalli, "Observation of the infrared properties of the ocean—implications for the measurement of sea surface temperature via satellite remote sensing," Bull. Am. Meteorol. Soc. **77,** 41–51 (1996).
24. X. Wu and W. L. Smith, "Emissivity of a rough sea surface for 8–13 μm: modeling and verification," Appl. Opt. **36,** 2609–2619 (1997).
25. P. D. Watts, M. R. Allen, and T. J. Nightingale, "Wind speed effects on sea surface emission and reflection for the Along Track Scanning Radiometer," J. Atmos. Oceanic Technol. **13,** 126–141 (1996).
26. C. Bourlier, "Unpolarized emissivity with shadow and multiple reflections from random rough surfaces in the geometric optics approximation. Application to Gaussian sea surfaces in the infrared band," Appl. Opt. **45,** 6241–6254 (2006).
27. K. Masuda, "Infrared sea surface emissivity including multiple reflection effect for isotropic Gaussian slope distribution model," Remote Sens. Environ. **103,** 488–496 (2006).
28. F. Losasso and H. Hoppe, "Geometry clipmaps: terrain rendering using nested regular grids," ACM SIGGRAPH Trans. Graph. **23,** 769–776 (2004).